JOURNAL OF GEOPHYSICAL RESEARCH, VOL. 104, NO. E2, PAGES 3815–3832, FEBRUARY 25, 1999

High Rayleigh number compressible convection in Venus' atmosphere: Penetration, entrainment, and turbulence

R. David Baker[1] and Gerald Schubert[2]

Department of Earth and Space Sciences, University of California, Los Angeles

Philip W. Jones

Los Alamos National Laboratory, Los Alamos, New Mexico

Abstract. Numerical simulations of two-dimensional, nonlinear fully compressible convection at the subsolar point in the clouds of Venus are presented. One moderate Rayleigh number case ($Ra_q = 6.8 \times 10^6$) and two high Rayleigh number ($Ra_q = 1.1 \times 10^9$) cases are considered. Cloud-level convection is characterized by cold, narrow downwellings that deeply penetrate the underlying stable layer and that entrain warmer air from the overlying stable layer. The convection layer depth, as determined from the horizontally averaged static stability, spans 9 km (47-56 km altitude) and 14 km (46-60 km altitude) for the moderate Rayleigh number and high Rayleigh number simulations, respectively. In the high Rayleigh number cases, convective penetration extends over a scale height from the bottom of the convection layer down to 38 km altitude. Strong convective entrainment completely erodes the overlying stable layer in the high Ra_q cases and incorporates it into the convection layer. The timescale for entrainment of the overlying stable layer is roughly 1 day and may explain why cellular features are predominantly found near and downwind of the subsolar point. The high Rayleigh number simulations are convectively turbulent and exhibit a spectral energy cascade of k^{-3}, where k is the horizontal wavenumber. Our results suggest that cellular features in the subsolar region are observed at the cloud tops because convection may extend to much higher altitudes there. Downward penetrative convection may also be responsible for turbulence observed in Venus' atmosphere at 45 km altitude.

1. Introduction

Penetrative convection strongly influences atmospheric dynamics in the clouds of Venus. Pioneer Venus and Vega 2 probes as well as Magellan radio occultation experiments detected a neutrally stable region from roughly 48 to 55 km altitude, bounded both above and below by stable layers [*Seiff et al.*, 1980; *Young et al.*, 1987; *Jenkins et al.*, 1994; *Hinson and Jenkins*, 1995]. This neutrally stable region is produced by convective mixing. However, the influence of cloud-level convection may extend far beyond the neutrally stable region. Previous simulations indicate that downflow plumes penetrate the underlying stable layer and generate internal gravity waves below the convection layer, while convective entrainment of the overlying stable layer generates gravity waves above [*Baker et al.*, 1998]. Penetration by deep convection may explain the large cellular features observed in ultraviolet images near the subsolar point [*Baker and Schubert*, 1992]. It may also force the global Y feature [*Gierasch*, 1987], generate small-scale gravity waves that may contribute to the mean flow [*Schinder et al.*, 1990; *Leroy and Ingersoll*, 1995], and induce variations in sulfuric acid concentration in the lower cloud region [*James et al.*, 1997; *Baker et al.*, 1998].

The large cellular features observed near the subsolar point in Mariner 10, Pioneer Venus, and Galileo ultraviolet images are located at cloud top heights of roughly 65 km altitude [*Murray et al.*, 1974; *Rossow et al.*, 1980; *Belton et al.*, 1991]. These cells are thought to be caused by thermal convection in the region [*Belton et al.*, 1976; *Covey and Schubert*, 1981; *Belton et al.*, 1991; *Baker and Schubert*, 1992]. Unfortunately, only coarse measurements of the thermal structure in the subsolar region have been performed (by Venera landers 10, 11,

[1]Now at NASA Goddard Space Flight Center, Universities Space Research Association, Greenbelt, Maryland.

[2]Also at Institute of Geophysics and Planetary Physics, University of California, Los Angeles.

Paper number 1998JE900029.
0148-0227/99/1998JE900029$09.00

and 12) and stability inferences from these data do not capture the fine stability structure [*Seiff*, 1983]. However, high-resolution observations of the thermal structure away from the subsolar point [*Seiff et al.*, 1980; *Young et al.*, 1987; *Jenkins et al.*, 1994; *Hinson and Jenkins*, 1995] indicate that the neutrally stable layer only reaches up to roughly 55 km altitude, 10 km below the cloud tops. Upward convective penetration has been proposed as a mechanism for producing the cloud top cells [*Belton et al.*, 1991; *Baker and Schubert*, 1992], but recent numerical simulations show that cloud-level convection is characterized by strong, narrow downwellings and that upward penetration is relatively weak [*Baker et al.*, 1998]. More vigorous convection might penetrate higher, a possibility we investigate below. Indeed, we will show that sufficiently vigorous convection does extend to much higher (and lower) altitudes in the subsolar region.

The numerical simulations of *Baker et al.* [1998] exhibit many interesting features. Cloud-level convection consists of cold, narrow downflow plumes that deeply penetrate the underlying stable layer (by as much as 5 km) and entrain air from the overlying stable layer. Penetration and entrainment widen the neutrally stable region by roughly 2 km and generate internal gravity waves in the stable layers. Convective downdrafts experience intense compressional heating as they penetrate into the underlying stable layer and also generate nonlinear "interfacial" waves within the penetrative region. This nonlinear response of the penetrative region may account for turbulence observed at 45 km altitude [*Woo et al.*, 1982]. Furthermore, the simulations suggest that the Vega balloons drifted in a relatively quiescent part of the convection layer. Calculated vertical velocities of 1-5 m s^{-1} at 54 km altitude (the average altitude of the Vega balloons) are consistent with Vega measurements, but much larger velocities (~11-14 m s^{-1}) occur in the lower part of the convection layer.

The purpose of this paper is to investigate the nature of high Rayleigh number convection in Venus' atmosphere. *Baker et al.* [1998] used a value of eddy diffusion of 155 m^2 s^{-1}, consistent with values inferred from radio scintillation experiments [*Leroy*, 1994]. The value of eddy diffusion deduced from photochemical modeling is 2 orders of magnitude smaller at roughly 2 m^2 s^{-1} [*Krasnopolsky and Parshev*, 1981, 1983; *Krasnopolsky*, 1985; *Yung and Demore*, 1982]. However, this value of eddy diffusion may not be appropriate for modeling small-scale turbulence since eddy diffusion in photochemical models also parameterizes large-scale dynamics. Nevertheless, smaller values of eddy diffusion (higher Rayleigh number) result in more vigorous convection and potentially more extensive penetration since less heat can be transported by small, turbulent eddies. In this paper, calculations of subsolar convection in Venus' atmosphere with eddy diffusion coefficients of 155 and 84 m^2 s^{-1} are presented. (The case presented here with an eddy diffusivity of 155 m^2 s^{-1} differs from the *Baker et al.* [1998] 100% subsolar heating case in horizontal extent only (60 km and 180 km, respectively).) The small reduction in eddy diffusion causes large differences in the extent of penetration and the character of convection in the subsolar region. We begin by presenting the model of Venus' atmosphere. The next section describes the results of our simulations, and the last section discusses the implications of these results for the subsolar region.

2. Model

The mathematical model of Venus' atmosphere and the numerical approach are fully described in the appendix. Briefly, we use a two-dimensional (2-D), nonlinear, fully compressible model of a perfect gas to simulate cloud-level convection from 35 to 60 km altitude. Full compressibility is required because cloud-level convection in Venus' atmosphere spans a scale height (~7 km at 50 km altitude) or more and local compressibility preferentially produces strong, narrow downwellings [*Hurlburt et al.*, 1984]. Variables in our model such as density, velocity, and potential temperature are decomposed into two components: a steady (at the timescales of our simulations) background state that is supported by processes such as thermal radiation and large-scale dynamics with timescales much longer than convection and waves, and time-dependent deviations from this background state that include convection and waves with timescales of seconds to hours. A Venus-like background stability profile similar to that used by *Young et al.* [1987] is adopted (Figure 1), and the background mean wind is zero. Time-dependent deviations (convection and gravity waves) are driven by absorption of solar radiation in the clouds. The simulations in this paper consider solar heating at the subsolar point (Fig-

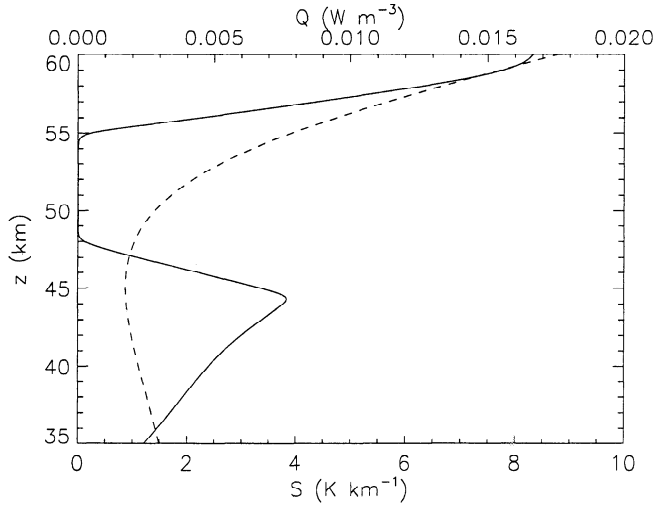

Figure 1. Static stability profile for the background state (solid) and subsolar heating profile (dashed) as a function of altitude.

Table 1. Input Parameters Different Among the Three Cases

	Case A	Case B	Case C
κ_m, $m^2 s^{-1}$	155.0	84.1	84.1
κ_θ, $m^2 s^{-1}$	155.0	84.1	84.1
d, km	20.0	20.0	25.0
Ra_q	6.8×10^6	1.1×10^9	1.1×10^9
Altitude, km	40-60	40-60	35-60
Δx, km	0.181	0.121	0.121
Δz, km	0.121	0.121	0.121

ure 1), the maximum solar heating possible in Venus' atmosphere. Subsolar heating is determined from extrapolation of Pioneer Venus solar flux measurements [*Tomasko et al.*, 1980]. Small-scale turbulence is modeled by eddy diffusion with a constant diffusion coefficient. The conservation equations of mass, momentum, and energy are solved explicitly using a time-adaptive leapfrog scheme for all but the diffusion terms, which are solved using an implicit Crank-Nicolson scheme and Jacobi iteration in the energy equation and an explicit time lag scheme in the momentum equations. Spatial derivatives are computed using centered, second-order differences on a vertically staggered grid. A frequency filter [*Asselin*, 1972] is applied at every time step to dampen the leapfrog computational mode.

The heating profile in Figure 1 shows the strongest heating near the top of the domain. At first, one may conclude that this heating profile provides a stabilizing influence on the atmosphere since the upper portions of the atmosphere warm faster than the lower portions. In fact, the subsolar heating provides a destabilizing influence on the atmosphere. Consider a simple uniformly internally heated system with an insulating lower boundary. By the argument above, this system should not convect because the bottom of the layer warms at the same rate as the top of the layer. However, convection does occur in this system if the critical Rayleigh number is exceeded [e.g., *Roberts*, 1967]. Destabilization occurs because a negative temperature gradient is established to transfer heat out of the system conductively.

Below 60 km altitude, the Venus atmosphere is radiatively opaque [*Hou and Goody*, 1989], and longwave radiative transfer can be modeled by a radiative diffusivity. In the calculations presented here, the values of eddy diffusivity (84 and 155 $m^2 s^{-1}$) are larger than the values of radiative diffusivity in Venus' atmosphere (1 $m^2 s^{-1}$ at 35 km altitude to 48 $m^2 s^{-1}$ at 60 km altitude). Because heat transfer is accomplished diffusively, a negative temperature gradient (destabilizing influence) must be established to transport heat upward. If heating occurs in a stable layer, the layer becomes less stable. If heating occurs in a neutrally stable layer, the layer becomes unstable, and convection ensues. Stronger destabilization (i.e., a more negative temperature gradient) occurs in regions where heating is larger. Thus, although heating is largest near the top of the domain, absorption of solar radiation exerts a destabilizing influence on the atmosphere below 60 km altitude. Above 60 km altitude, radiation to space becomes dominant and longwave radiation can no longer be modeled as a diffusive process. In this situation, a heating profile with a positive gradient (larger heating values at larger altitudes) may produce a stable atmosphere.

We consider three cases in this paper. Each simulation represents a quasi-steady solution that captures, in a statistical sense, the potential response of the subsolar atmosphere to the large solar forcing at the subsolar point. Table 1 lists input parameters that vary among the three cases. Here, κ_m is eddy momentum diffusivity, κ_θ is eddy thermal diffusivity, d is the total depth, Ra_q is the internally heated Rayleigh number defined below, Δx is the horizontal grid spacing, and Δz is the vertical grid spacing. The essential difference among the three cases is the value of eddy diffusion and the vertical extent of the computational domain. Cases A and B differ in eddy diffusion (155 and 84 $m^2 s^{-1}$, respectively), while cases B and C differ in vertical extent (40-60 km altitude and 35-60 km altitude, respectively). The horizontal extent is 60 km for all three cases.

The internally heated Rayleigh number Ra_q is the ratio of buoyancy forces due to internal heat generation to viscous forces:

$$Ra_q = \frac{g q_0 d^{*5}}{T_0 \rho_0 c_p \kappa_\theta^2 \kappa_m} \quad (1)$$

Here, g is the acceleration of gravity (8.87 m s^{-2}), q_0 is the volumetric solar heating at the reference level, d^* represents the convection layer depth, T_0 is the reference level temperature, ρ_0 is the reference level density, and c_p is specific heat at constant pressure. The reference level is located at the top of the convection layer (different for each case) where solar heating is greatest. The convection layer depth d^* and the reference level are determined a posteriori. As we shall see, convective penetration and entrainment widen the convection layer from its background state thickness. Thus, Rayleigh numbers based on the thickness of the background state neutrally stable layer inadequately represent the convective state of these calculations. For case A, the convection layer extends from 47 to 56 km altitude. For cases B and C, the convection layer spans from 46 to 60 km altitude. The combination of reduced values of eddy diffusion and increased convection layer thickness results in a much higher Rayleigh number for cases B and C as compared to case A.

The horizontal boundaries are stress-free with a fixed heat flux and the side boundaries are periodic. Impermeable, stress-free boundaries cause artificial wave reflection and an intensification of gravity wave ampli-

tudes in the stable layers. However, *Baker et al.* [1998] have shown that the artificially trapped gravity waves do not significantly alter the convection. The value of heat flux at the boundaries is equal to but opposite in sign from the solar flux at that level.

Cases A and B are started from the 100% subsolar heating solution of *Baker et al.* [1998]. The input parameters for the *Baker et al.* [1998] 100% subsolar heating case are identical to case A except for a larger horizontal extent of 180 km. The final solution of *Baker et al.* [1998], from 0 to 60 km horizontally, is used to initialize cases A and B. The initial condition for case C is the final solution of case B from 40 to 60 km altitude plus a motionless, conductive state from 35 to 40 km altitude. Since our model includes sound waves, a small time step of roughly 0.12 s is required to meet the Courant condition for stability. Cases A, B, and C are integrated for 13.8, 74.9, and 17.9 simulation hours, respectively. Case B remains in the transient phase (a state in which the mean kinetic energy exhibits long-term growth or decay) for ~51.2 simulation hours during which the overlying stable layer is eroded away by convective entrainment. The nontransient, statistically steady (i.e., when the mean kinetic energy does not exhibit a secular trend) integration time for the three cases is 12.1, 23.7, and 11.4 hours, respectively. For the remainder of the paper, time $t = 0$ marks the beginning of the nontransient phase.

3. Results

3.1. Penetration and Entrainment

Plate 1a shows total potential temperature at one instant in time for the moderate Ra_q simulation (case A), where x is horizontal distance and z is altitude. The flow is highly time-dependent (Figure 2); the images in Plate 1 occur during a peak in kinetic energy density. For case A, cloud-level convection occurs from roughly 47 to 56 km altitude with stable layers located both above and below the convection layer. Convection is characterized by cold, narrow downwellings with widths of 1-2 km. Strong downwellings form at the top of the convection layer by a merging of weaker downwellings. The plume located at $x = 56$ km is an example of a recently merged downwelling. Downdrafts deeply penetrate the underlying stable layer and generate waves below the convection layer. The wave structure is most easily seen in this figure at the interface between the convection layer and the underlying stable layer. We refer the reader to *Baker et al.* [1998] for a discussion of these wave features. Typical downdraft velocities are roughly 8-11 m s^{-1} with higher downward velocities (maximum downward velocity of 14.6 m s^{-1}) occurring just above the underlying stable layer. The stable layer mechanically forces the downdraft air upward. For example, the downwelling located at $x = 15$ km began penetration of the stable layer roughly 10 minutes earlier. As seen in this image, part of this plume has now splashed upward and to the right. Upward mechanical forcing by the underlying stable layer produces the largest upward velocities in this simulation, with typical upward velocities of roughly 3-6 m s^{-1} and a maximum value of 9.0 m s^{-1}.

A striking difference in convective style and convection layer depth occurs for the high Ra_q simulation, case B (Plate 1b). The convection layer depth now extends from 46 to 60 km altitude. The initial condition for case B includes both stable layers, but convective entrainment has now completely incorporated the overlying stable layer. Narrow downwellings also dominate the convective planform in case B with horizontal widths of 1-4 km. Penetration into the underlying stable layer by convective downdrafts is deeper (the extent of penetration will be quantified later), and wave features again can be seen at the interface between the convection layer and the underlying stable layer. Typical downdraft velocities are roughly 9-13 m s^{-1} with a maximum downward velocity of 16.0 m s^{-1}. More vigorous motion occurs in the high Ra_q simulation. The maximum upward velocities in this simulation (18.0 m s^{-1}) occur within the vortex located at $x = 7$ km. Case C (not shown in Plate 1) exhibits similar behavior as case B, with deep convection again occurring from 46 to 60 km altitude.

Many interesting features occur near the major downwelling at $x = 10$ km in Plate 1b. The downflow plume consists of cold air separated by warmer air in the center. The warm, buoyant air is forced downward by the adjacent downdrafts and travels the entire depth of the convection layer. The bubble of warm air located above the downdraft from 59 to 60 km altitude collects due to strong convergence and compressive heating in the upper portion of the convection layer. When the downwelling becomes less intense a few hours later (Figure 2), convergence weakens and this pool of warm air mixes with cooler air. Vortices associated with downflow plumes are rather large, spanning over a scale height from 43 to 53 km altitude. The vortices efficiently mix air from the underlying stable layer with air from the convection layer. Entrainment of underlying stable air by plume vortices can be seen at ($x = 1$ km, $z = 49$ km) and ($x = 20$ km, $z = 49$ km).

Figure 2 shows the time series of the domain-averaged kinetic energy density for all three cases. All three cases are strongly time-dependent. Spectral analysis of the kinetic energy density time series indicates dominant periods of roughly 160 min and 65 min for case A; 300 min, 160 min, and 70 min for case B; and 230 min and 49 min for case C (Figure 3). The long period oscillations in kinetic energy are associated with the convective overturning time of convection cells with horizontal scales of roughly 30 km. Even though the convective velocities are smaller for the moderate Ra_q simulation than for the high Ra_q simulations, the convective

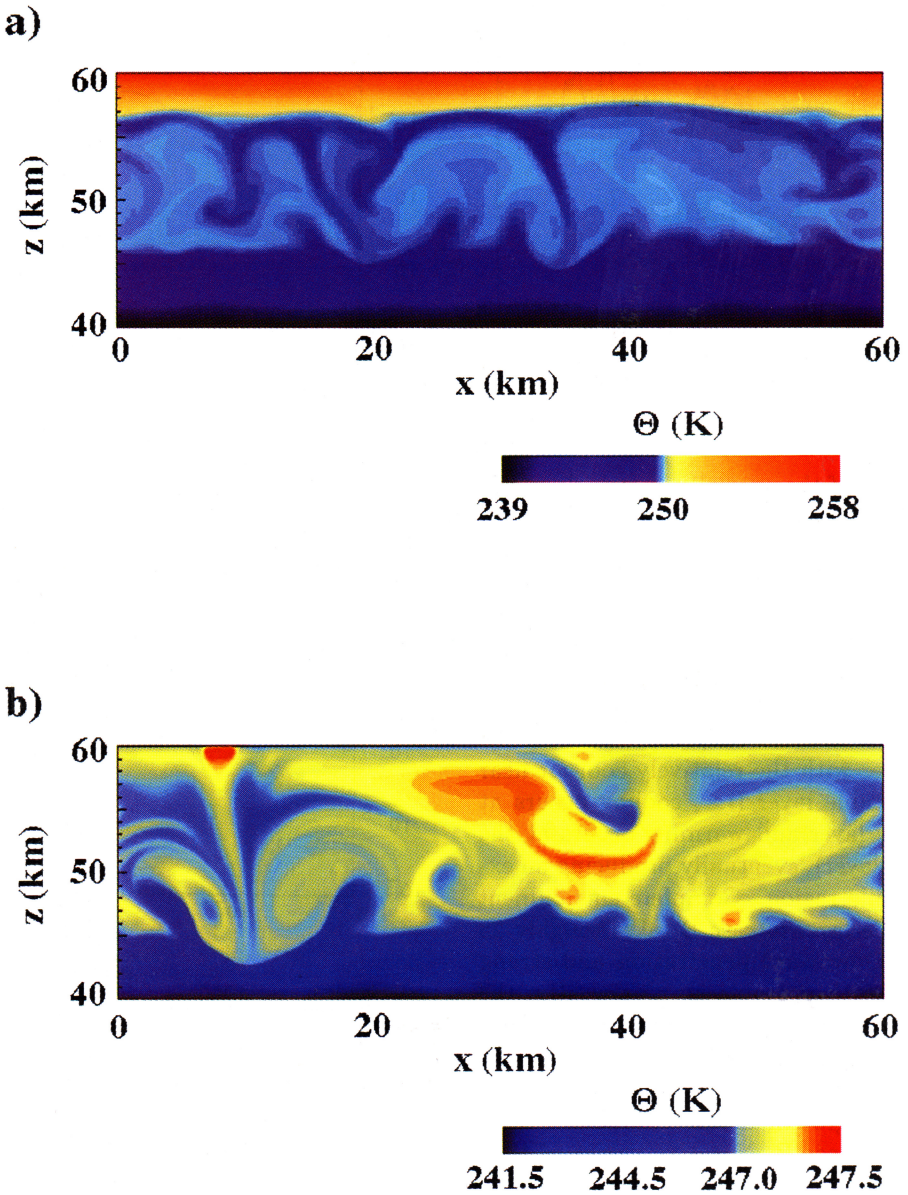

Plate 1. Snapshots of potential temperature at a peak in kinetic energy density for (a) $Ra_Q = 6.8 \times 10^6$ (case A) and (b) $Ra_Q = 1.1 \times 10^9$ (case B). The snapshots occur at time (a) $t = 10.35$ hours and (b) $t = 3.39$ hours. The color map is slightly different between the two cases to maximize contrast.

overturning time is shorter because the convection layer depth is smaller. Kinetic energy oscillations with periods of roughly 50-70 min are related to a penetrative timescale controlled by merging of weak downwellings into stronger downwellings. The high Ra_q simulations also experience relatively rapid oscillations with periods of roughly 15-30 min associated with smaller scale eddies and plume vortices. Case B has the highest average kinetic energy density because most of the domain is convectively active. The average kinetic energy density in case C is slightly lower than in case B because the additional vertical extent in case C from 35 to 40 km altitude is stable. Case A has the lowest average kinetic energy density because less of the domain is convectively active and the convective velocities are smaller.

Convective penetration and entrainment deepen the neutrally stable region (Figure 4). The horizontally averaged neutrally stable region spans from 47 to 56 km altitude in the moderate Ra_q case (2 km thicker than the background state) and from roughly 46 to 60 km altitude in cases B and C (7 km thicker than the background state). The overlying stable layer is substantially weakened in the moderate Ra_q case and virtually eroded away in the high Ra_q cases by solar heating and convective entrainment. The lower value of eddy diffusivity in the high Ra_q cases results in less heat transport by small-scale turbulent eddies. The decrease in

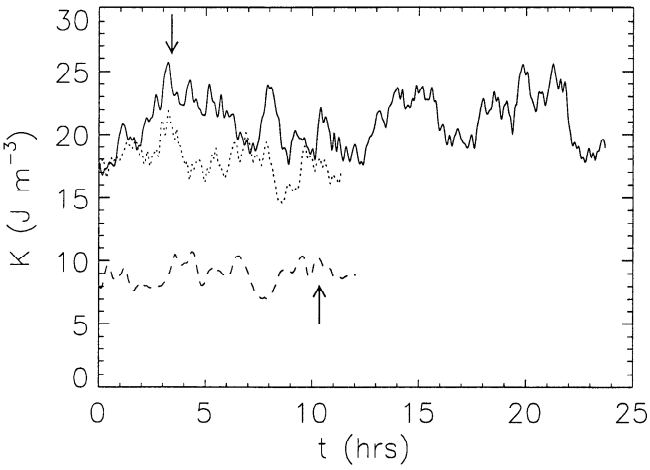

Figure 2. Time series of the spatially averaged kinetic energy density over the entire computational domain for case A (dashed), case B (solid), and case C (dotted). Arrows indicate location of snapshots shown in Plate 1.

small-scale turbulent transport causes heat to build up in the overlying stable layer. This heat is eventually transferred by larger-scale convective motions. Convective entrainment mixes the relatively warm air near the top of the stable layer with the relatively cool air near the bottom of the stable layer (i.e., cooling occurs at the top of the stable layer and warming occurs at the bottom of the stable layer), eventually producing an extended neutrally stable region. Complete entrainment of the overlying stable layer in case B takes roughly 25 hours (Figure 5). Downward penetration and strong mixing of stable air with unstable air also weaken the underlying stable layer. Because penetration is deeper in the high Ra_q cases, the maximum stability of the underlying stable layer occurs at a lower altitude.

Figure 5 shows the growth of the convection layer thickness over time in case B. Negative values of time represent the transient phase of the simulation as determined from the time series of spatially averaged kinetic energy. Because of strong convective penetration and entrainment, the precise altitudes of the upper and lower boundaries of the convection layer are somewhat ambiguous. We define the transition from the convection layer to the stable layer as the vertical level where the horizontally averaged static stability first exceeds the small value of 0.05 K km^{-1}. As Figure 5 shows, the convection layer thickness in case B increases from 9 km to 14 km (recall that the initial condition for case B included a stable layer above 56 km altitude). Entrainment of the overlying stable layer occurs early in the simulation until the top of the convection layer reaches the domain boundary at 60 km altitude. Even though the convection layer extends to 60 km altitude after approximately 25 hours, the transient phase lasts an additional 26 hours during which deep convection more fully develops. Occasional sharp dips in the altitude of the convection layer upper boundary denote the presence of

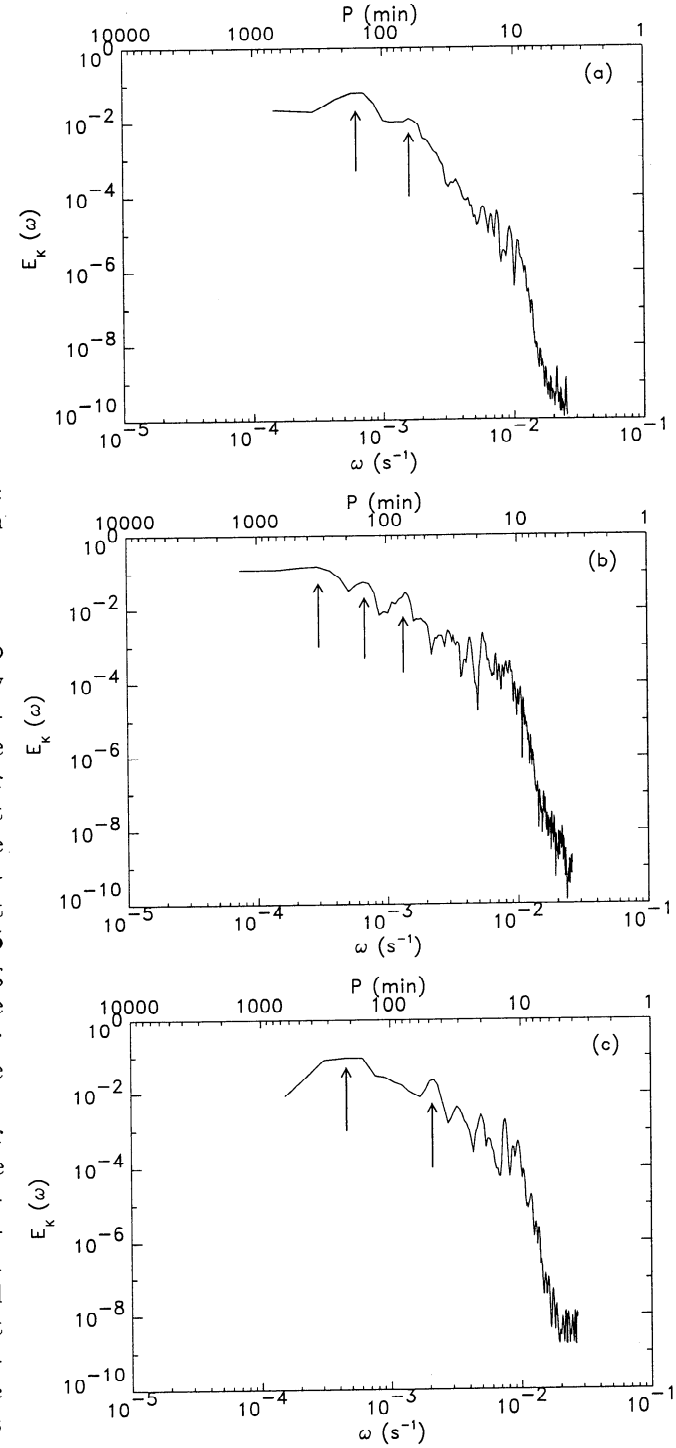

Figure 3. Power spectral density E_K of spatially averaged kinetic energy density as a function of angular frequency ω and period P for cases A–C. Arrows indicate dominant peaks discussed in the text. The units of E_K are J^2 m^6 s^{-1}.

a small, temporary stable layer produced by transient hot bubbles near 60 km altitude (Plate 1b). Strong convective penetration extends the lower boundary of the convection layer to 46 km altitude over a timescale of a few days (here, a day equals 24 hours rather than

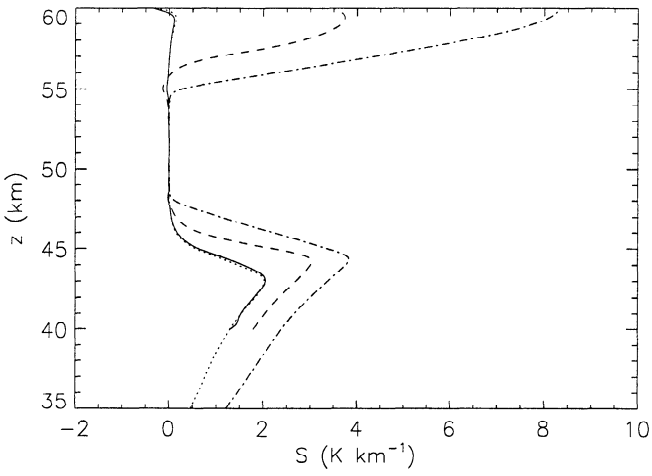

Figure 4. Time-averaged, horizontally averaged static stability as a function of altitude for case A (dashed), case B (solid), and case C (dotted). The background static stability is given by the dash-dot line. The static stability profiles for cases A and B do not extend below 40 km altitude, the lower boundary for the cases.

a Venus solar day). Rapid variations in the altitude of the convection layer lower boundary illustrate the strong time-dependence of penetrative convection.

The entrainment velocity w_e (the growth rate of the convection layer by convective entrainment) is given by [*Stull*, 1988]

$$w_e = \frac{A\overline{w'\theta'}}{\Delta\overline{\theta_e}} \tag{2}$$

where A is an empirically determined constant, w is vertical velocity, and θ is potential temperature. An overbar indicates a horizontal average and primed quantities are deviations from the horizontally averaged value. $\Delta\overline{\theta_e}$ represents the horizontally averaged potential temperature increase across the entrainment zone. A value of $A = 0.2$ is typically used for boundary layer convection in Earth's atmosphere [*Stull*, 1976] and will also be employed here. Initially for case B, the entrainment zone is roughly 1 km thick and the static stability in the entrainment zone is approximately 1 K km^{-1}, thus giving a value of $\Delta\overline{\theta_e} \approx 1.0$ K. For values at 56 km altitude of $F_c = 130$ W m^{-2} ($\overline{w'\theta'}$ is related to F_c in (3) below), $\rho = 0.77$ kg m^{-3}, and $c_p = 890$ J kg^{-1} K^{-1}, we obtain an entrainment velocity w_e from (2) of roughly 0.04 m s^{-1}. This value of w_e agrees quite well with the growth rate observed in Figure 5 (convection layer growth of 4.0 km over 25 hours gives an entrainment velocity of 0.044 m s^{-1}).

The upper boundary at 60 km altitude obviously affects the high Rayleigh number solutions. Vertical growth of the convection layer by entrainment is limited by the upper boundary in cases B and C. Positively buoyant warm bubbles near the upper boundary (Plate 1b) would penetrate into the overlying stable layer if the fixed upper boundary at 60 km altitude were relaxed. In addition, the upper boundary may cause downward penetration to be slightly deeper in extent. *Hurlburt et al.* [1986] found that a two-layer system (convection layer and underlying stable layer) captures the main dynamical features of a three-layer system (convection layer between two stable layers) but that downward convective penetration is roughly 7% deeper in the two-layer case. These considerations suggest that a case with the upper boundary located above 60 km altitude should be performed to determine the true extent of convective entrainment and penetration within the cloud region. Above 60 km altitude, the radiative timescale is comparable to the convective timescale [*Pollack and Young*, 1975; *Hou and Goody*, 1989]. Thus thermal radiation will act to reduce thermal fluctuations above 60 km altitude associated with convection. Our model currently does not include this radiative damping effect, and therefore a convection simulation with an upper boundary above 60 km altitude would exhibit more vigorous convective (and wave) motions above this altitude than would be present in the real Venus atmosphere. Convective entrainment in the simulation would be unrealistically strong above 60 km altitude, and thus the extent of convective entrainment could not be accurately determined. Incorporation of radiative damping into the model is necessary before calculations above 60 km altitude can be performed.

The extent of downward penetration can be determined from the convective heat flux F_c:

$$F_c = \overline{\rho c_p w'\theta'} \tag{3}$$

where ρ is density. Positive values of F_c indicate upward heat transport by convection and negative values

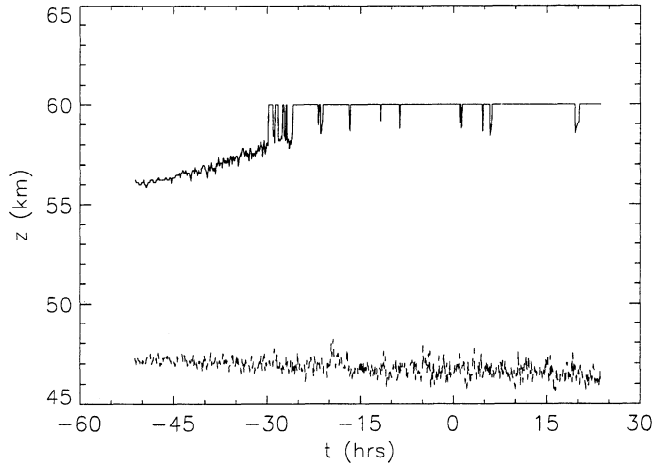

Figure 5. The altitudes of the top of the convection layer (solid) and the bottom of the convection layer (dashed) versus time for case B. Negative values of time indicate the transient phase of the simulation. The upper boundary of the calculation domain is at 60 km altitude.

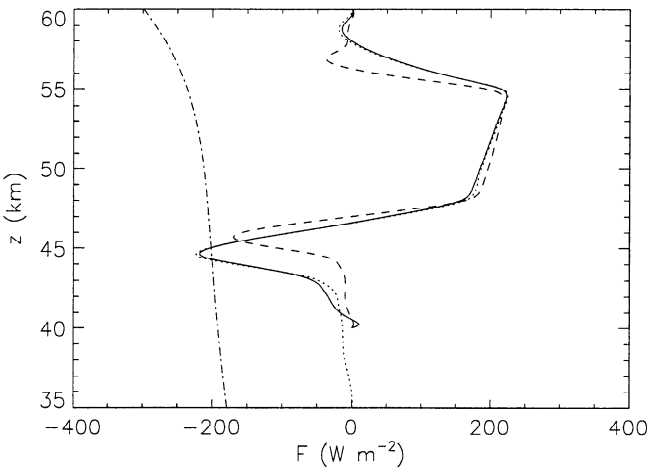

Figure 6. Time-averaged convective heat flux F_c as a function of altitude for case A (dashed), case B (solid), and case C (dotted). The solar heat flux at the subsolar point (dash-dot) is also plotted.

indicate regions of penetration or entrainment (e.g., relatively warm air transported downward by convective downwellings). Figure 6 shows the time-averaged convective heat flux for all three cases. The high Ra_q cases exhibit stronger, deeper penetration than the moderate Ra_q case. Average penetration extends to 42.7 km and 40.7 km altitude for cases A and B, respectively. The domain boundary at 40 km altitude limits the extent of penetration in case B; case C experiences average penetration down to roughly 38.0 km altitude. In addition, the amount of heat transferred downward by convective penetration at 45 km altitude is comparable to the solar heat flux. Convective penetration may thus operate as a significant heat source in the underlying stable layer. Convective heating (divergence of the convective heat flux) due to convective penetration is largely balanced by cooling due to divergence of eddy diffusive heat flux [*Baker et al.*, 1998]. Thus heating from convective penetration results in increased small-scale turbulence in the penetrative region. Convective entrainment can be seen near the upper boundary in all three cases. Entrainment appears stronger in case A than in cases B and C because there is little stable air left to entrain in the high Ra_q cases (i.e., entrainment has already incorporated the overlying stable layer into the convection layer.)

The effect of compressibility in these simulations can be illustrated by the horizontally averaged pressure work W_p:

$$W_p = -\overline{p'\nabla \cdot \mathbf{v}'} \tag{4}$$

where p is pressure and $\mathbf{v}$ is velocity. W_p represents the work done to modify the volume of a given fluid element as it moves vertically; negative values of W_p tend to increase kinetic energy [e.g., *Chandrasekhar*, 1961]. This term vanishes in the Boussinesq approximation since the flow is nondivergent ($\nabla \cdot \mathbf{v}' = 0$ in the Boussinesq approximation). Figure 7 shows W_p at a peak in kinetic energy density for cases A and B corresponding to the same times depicted in Plate 1 and indicated by the arrows in Figure 2. Negative values of W_p occur in the convection layer, while positive values of W_p exist in the penetrative region. Thus, pressure work acts to increase the kinetic energy in the convection layer and tends to decrease the kinetic energy in the penetrative region. Near the top of the domain, W_p is positive for case A because the overlying stable layer acts to diminish kinetic energy, but W_p is negative in this region for case B since the overlying stable layer has been incorporated into the convection layer. Positive pressure work in the penetrative region represents the compression of penetrating plume heads by the underlying stable layer. The magnitude of W_p is slightly larger in the high Ra_q case, but both cases exhibit values of pressure work in the penetrative region comparable to the amount of solar heating in the lower stable layer (Figure 1). Because most of the pressure work in the penetrative region occurs near downwelling plume heads, local values of pressure work near penetrative plumes are even larger (~0.06 and ~0.2 W m^{-3} for cases A and B, respectively). These local compressional features may be responsible for turbulence observed at 45 km altitude by radio occultation experiments [*Woo et al.*, 1982], a point we discuss in more detail below.

3.2. Turbulence

High frequency oscillations in the time series of kinetic energy density for the high Ra_q simulations (Figure 2) suggest the possibility of turbulent motions. Figure 8 shows the time-averaged power spectra of vertical velocity and potential temperature at 52 km alti-

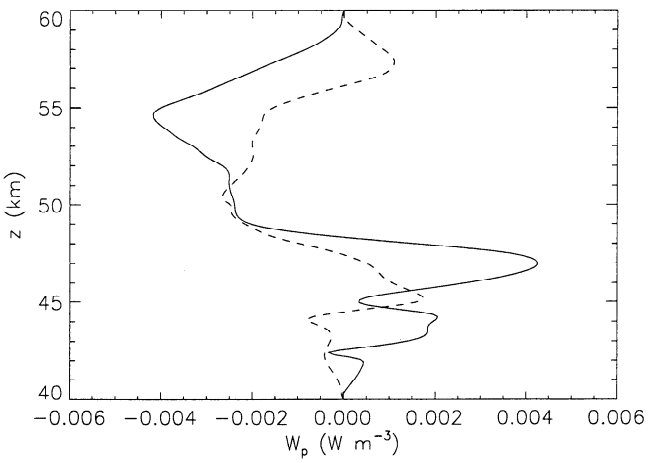

Figure 7. Pressure work W_p as a function of altitude at a peak in kinetic energy density for case A (dashed) and case B (solid) corresponding to the same times as shown in Plate 1.

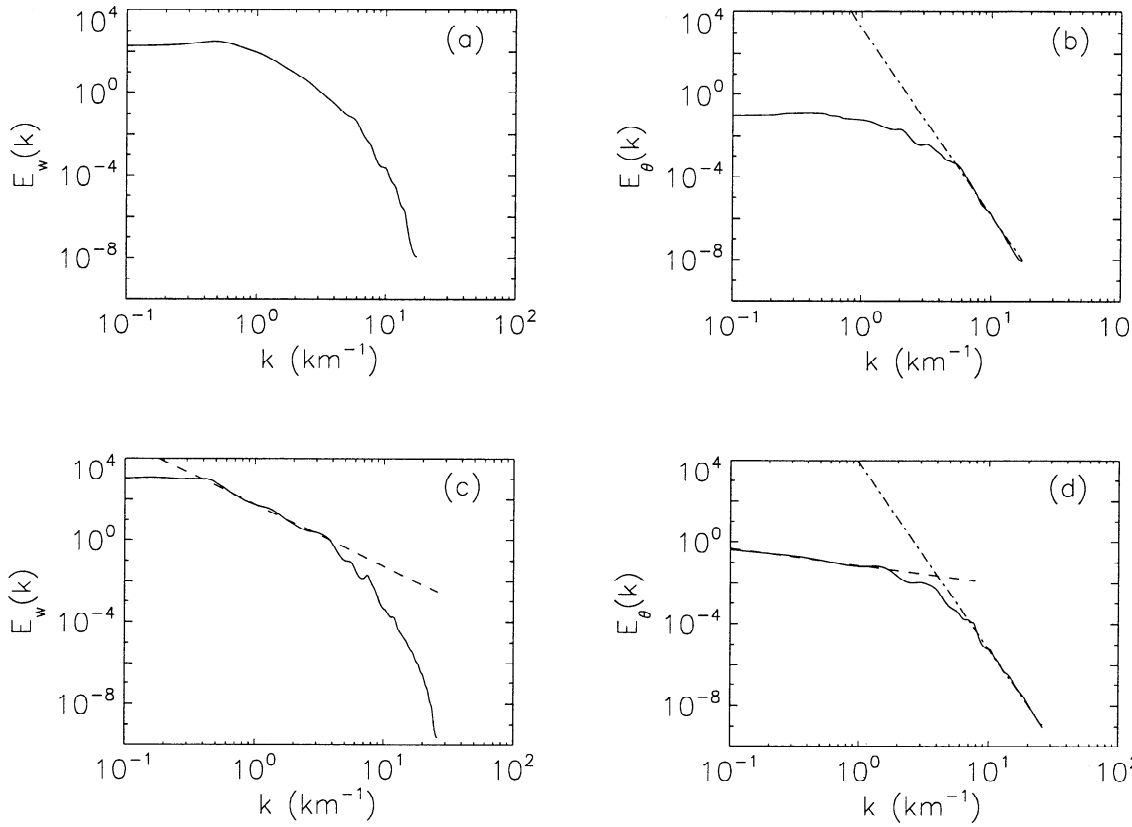

Figure 8. Time-averaged power spectral density at 52 km altitude of (a) vertical velocity, case A, (b) potential temperature, case A, (c) vertical velocity, case B, and (d) potential temperature, case B. The dashed lines in Figures 8c and 8d represent a least squares power law fit for low to intermediate wavenumbers with exponent values of -3.03 and -0.822, respectively. The dash-dot lines are high wavenumber least squares power law fits with exponents of (b) -9.09 and (d) -9.52. Power spectral density units for Figures 8a and 8c are in $m^2\ s^{-2}$ km, while the units for Figures 8b and 8d are in K^2 km.

tude as a function of horizontal wavenumber k for cases A and B. The high Ra_q vertical velocity spectrum exhibits a k^{-3} power law at moderate wavenumber with a steeper fall-off at high wavenumber, while the high Ra_q potential temperature spectrum shows a $k^{-0.8}$ power law relationship at low k and a steep fall-off at high k. (A k^{-3} relationship may be forming in the high Ra_q potential temperature spectrum at intermediate k, but the wavenumber range is somewhat limited.) The moderate Ra_q spectra show only a steep fall-off at high wavenumber. To further illustrate the power law relationships, we fit the logarithm of each power spectrum with a high-order polynomial to smooth the spectrum and then determined the slope of the polynomial fit in log space. Figure 9 shows the resulting power law exponent (exponential slope) as a function of horizontal wavenumber for the four power spectra. Again, we see that the high Ra_q case exhibits a k^{-3} power law in vertical velocity spectral energy over a decade of intermediate wavenumbers, a $k^{-0.8}$ power law in potential temperature spectral energy at low wavenumbers, and a steep power law ($\sim k^{-9}$) in potential temperature spectral energy at high wavenumbers. The waviness of the slopes at low wavenumber is likely caused by spurious oscillations produced by the polynomial fit.

Two-dimensional (2-D) isotropic turbulence follows a k^{-3} power law at wavenumbers larger than the wavenumber of forcing [*Kraichnan*, 1967; *Lilly*, 1969]. However, the k^{-3} behavior for the high Ra_q simulation also agrees with laboratory experiments of turbulent convection [*Kotsovinos*, 1991], recent numerical simulations of 3-D Boussinesq turbulent convection [*Kerr*, 1996], and large-eddy simulations of Earth's convective boundary layer [*Mason*, 1989]. Is the k^{-3} behavior exhibited by the high Ra_q simulation then caused by two-dimensionality or convection? *Lilly* [1969] considered a prescribed monochromatic forcing at k_f to drive 2-D turbulent motions. For wavenumbers less than k_f, the spectrum follows a $k^{-5/3}$ relationship (an energy anticascade). A k^{-3} spectrum occurs for wavenumbers larger than k_f. Also, polychromatic forcing complicates the 2-D energy spectrum. For turbulent forcing between wavenumbers k_{f1} and k_{f2}, the spectrum exhibits a $k^{-5/3}$ relationship for $k \leq k_{f1}$, k^{-3} behavior for $k \geq k_{f2}$, and no discernible power law between k_{f1} and k_{f2} [*Shao and Randall*, 1996]. As we show below,

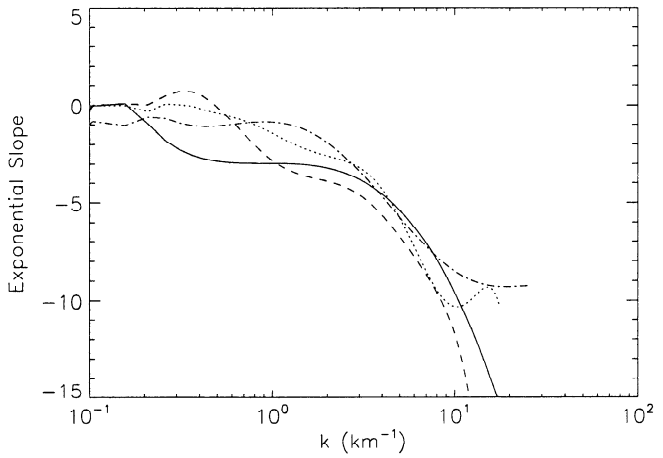

Figure 9. Power law exponent determined from polynomial fits of power spectra as a function of horizontal wavenumber for case A vertical velocity (dashed), case A potential temperature (dotted), case B vertical velocity (solid), and case B potential temperature (dash-dot).

the buoyant forcing in our simulations is distinctly polychromatic and the k^{-3} power law behavior falls within the wavenumber range of this forcing, thus implying that the k^{-3} spectral behavior is most likely the result of convective turbulence rather than two-dimensionality.

Consider the 3-D Boussinesq vorticity equation [*Emanuel*, 1994]:

$$\frac{d\omega}{dt} = \boldsymbol{\omega} \cdot \nabla \mathbf{v} - \nabla \times (\frac{\rho'}{\rho} g\hat{\mathbf{k}}) + \nu \nabla^2 \boldsymbol{\omega} \qquad (5)$$

where d/dt is the material time derivative, $\boldsymbol{\omega}$ is the vorticity, $\mathbf{v}$ is the velocity, ν is the kinematic viscosity, and $\hat{\mathbf{k}}$ is the unit vector in the vertical direction. Even though our simulations are fully compressible, the Boussinesq vorticity equation provides insight into turbulence generation in our model. The first term on the right side of (5) represents vorticity generation and destruction by vortex tilting and stretching, the second term on the right side represents vorticity generation by buoyancy, and the last term represents vorticity destruction by diffusion. For 2-D systems, the vortex tilting and stretching term is zero. Since diffusion acts primarily on high wavenumber features, the buoyancy term is responsible for vorticity generation and dissipation in the intermediate wavenumber range, i.e., buoyancy is the forcing mechanism for turbulent motions.

The buoyancy term in (5) for a 2-D system is given by

$$B = \frac{\partial}{\partial x}(\frac{\rho'}{\rho} g) \qquad (6)$$

Figure 10 shows time-averaged spectral power of B at 52 km altitude for case B. Clearly, vorticity forcing by buoyancy is polychromatic with broad forcing between roughly $k = 1$ km^{-1} and $k = 4$ km^{-1}. Furthermore, this polychromatic forcing is located at wavenumbers where the k^{-3} behavior occurs (Figure 8c). If the power law cascade of energy were caused by two-dimensionality alone, we would expect to find the k^{-3} behavior only for wavenumbers larger than $k = 4$ km^{-1}. Similarly, a -5/3 anticascade at wavenumbers smaller than $k = 1$ km^{-1} would occur if 2-D turbulence were dominant. A 2-D anticascade of energy possibly appears at low k in Figure 8d, but the spectral energy relationship ($\sim k^{-0.8}$) is much less steep than $k^{-5/3}$.

Under the assumption that buoyancy is the dominant process for generation and dissipation of turbulence at intermediate wavenumbers (the buoyancy subrange), dimensional analysis yields [*Lumley*, 1964; *Turner*, 1973]

$$E(k) \propto k^{-3} \qquad (7)$$

where $E(k)$ is the velocity power spectral density. This relationship has been previously used to describe the cascade of energy in a stably stratified fluid [*Lumley*, 1964; *Turner*, 1973], but our simulations suggest that this relationship also holds in the buoyancy subrange for an unstably stratified fluid. In addition, *Kotsovinos* [1991] argues through dimensional analysis that turbulent fluctuations in temperature in a convective plume follow k^{-3} in the buoyancy subrange.

Substantial power with a relatively flat spectrum occurs at low wavenumbers in Figure 8. Large power at low k is the consequence of periodic lateral boundary conditions in our model, that is, the power spectrum shows variation at the largest length scale of the computational domain. The flatness of the moderate Ra_q spectra at low k indicates that a 2-D anticascade of energy does not occur in the moderate Ra_q simulation. However, the $k^{-0.8}$ behavior at low k for the high Ra_q potential temperature spectrum suggests that a 2-D anticascade of energy may exist in the high Ra_q simulation. As noted above, the low wavenumber slope is less steep than for fully developed 2-D turbulence.

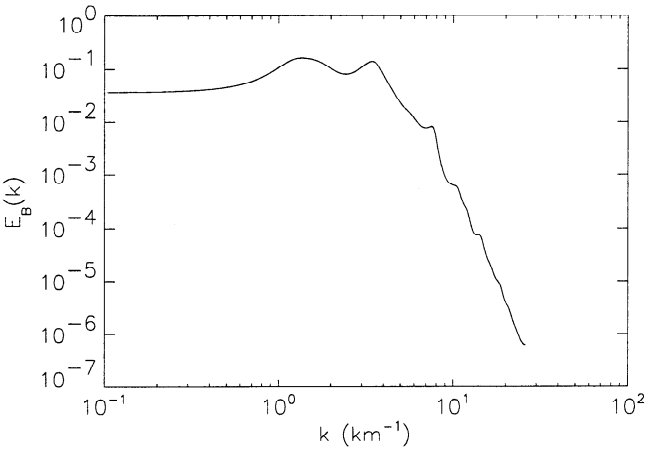

Figure 10. Time-averaged power spectral density at 52 km altitude of vorticity forcing by buoyancy E_B for case B. Power spectral density units are in s^{-4} km. Values of E_B have been multiplied by 10^9.

The steep fall-off of power at high k illustrates a weakness in parameterizing small-scale turbulent eddies by simple eddy diffusion [*Berkowicz*, 1984]. Isotropic turbulence exhibits an energy cascade of $k^{-5/3}$ in the inertial subrange [*Kolmogorov*, 1941], but our simulations show much steeper power law behavior (k^{-9}) in the "inertial subrange." Indeed, our high k spectra agree more closely with high wavenumber kinetic energy spectra in Earth's mesosphere controlled by molecular diffusion with a power law of k^{-7} [*Blix et al.*, 1990]. This result is not surprising since our eddy diffusion parameterization is analogous in form to molecular viscosity.

In summary, the k^{-3} spectrum exhibited in case B occurs for a wavenumber range that overlaps with dominant buoyancy-forcing wavenumbers. If 2-D turbulence were responsible for the energy cascade, the k^{-3} behavior would occur only for wavenumbers larger than the highest forcing wavenumber. In contrast, convective turbulence produces k^{-3} power law behavior within the buoyancy subrange. We therefore conclude that the turbulent structure in the high Ra_q simulation is likely caused by convective turbulence.

4. Discussion

Numerical simulations of nonlinear, fully compressible convection have been performed to investigate cloud-level convective penetration and entrainment in Venus' atmosphere. Three cases are presented: case A is a moderate Rayleigh number ($Ra_q = 6.8 \times 10^6$) calculation from 40 to 60 km altitude, case B is a high Rayleigh number ($Ra_q = 1.1 \times 10^9$) calculation from 40 to 60 km altitude, and case C is a high Rayleigh number ($Ra_q = 1.1 \times 10^9$) calculation from 35 to 60 km altitude. Cloud-level convection is characterized by cold, narrow downwellings. For the moderate Ra_q simulation, downflow plumes have widths of roughly 1-2 km and typical downdraft velocities of 8-11 m s^{-1} with maximum velocities of ~15 m s^{-1} near the underlying stable layer. The convective overturning time for the moderate Ra_q case is roughly 3 hours with a secondary penetrative timescale of roughly 1 hour associated with mergers of weaker downwellings into strong downdrafts. The horizontal extent of convection cells is roughly 10-30 km. In contrast, the high Ra_q simulations experience more vigorous convection. Downflow plumes with widths of 1-4 km exhibit downward velocities of 9-13 m s^{-1}. However, the maximum velocity in these simulations (upward velocity of 18 m s^{-1}) occurs in the plume vortex rather than in the penetrative downwelling. The high Ra_q simulations experience convective overturning times of roughly 4-5 hours, penetrative timescales of roughly 1 hour, and plume vortex timescales of 15-30 min. The plume vortices can be quite large, often spanning over a scale height vertically. An increase in the depth of the convection layer causes the larger convective overturning time for the high Ra_q cases. The width of the convection cells (~15–45 km) is slightly larger than for the moderate Ra_q case yet the aspect ratio of the cells remains similar for all three cases.

The horizontal scale of convection cells (~15–45 km) in our simulations is an order of magnitude smaller than the horizontal scale of the large cellular features (~200–1000 km) observed in the subsolar region [*Murray et al.*, 1974; *Rossow et al.*, 1980; *Belton et al.*, 1991; *Baker and Schubert*, 1992; *Toigo et al.*, 1994]. Although only 60 km wide, the horizontal domain in our simulations does not limit the horizontal scale of the simulated convection cells [*Baker et al.*, 1998]. There is observational evidence in Mariner 10 and Galileo ultraviolet images of smaller, transient cells with diameters of 50–100 km [*Murray et al.*, 1974; *Toigo et al.*, 1994]. The smallest resolvable convection cells in the UV images would have diameters of 30–60 km, and therefore the small-scale convection cells suggested by our model simulations to exist in Venus' atmosphere are at the limit of resolvable features. Larger cellular features with horizontal scales of 200–1000 km could be a mesoscale organization of individual convection cells with characteristic sizes of 15–45 km. Indeed, mesoscale convective complexes in Earth's atmosphere with horizontal scales of 100–300 km are comprised of individual thunderstorms with horizontal scales of roughly 10–30 km [*Maddox*, 1980].

Entrainment of air from the overlying stable layer can significantly increase the convection layer depth. The high Ra_q calculations display convection layer depths of 14 km, roughly two scale heights at the cloud level. Even though downward convective penetration is intense, this deep convection develops primarily through entrainment of overlying stable air by convective downwellings. The overlying stable layer from 56 to 60 km altitude is completely eroded away by convective entrainment with a timescale of roughly one day. The domain boundary at 60 km altitude limits the extent of convective entrainment in our simulations, and it is entirely feasible that erosion of the stable layer would continue above 60 km altitude. Since the radiative timescale in the Venus atmosphere becomes comparable to the convective timescale above 60 km altitude [*Pollack and Young*, 1975], thermal radiation would tend to reduce thermal fluctuations associated with convection. Currently, our model does not include this radiative damping effect. A simulation using the current model with the upper boundary located above 60 km altitude thus would not capture essential physics in Venus' middle atmosphere. Nevertheless, it seems unlikely that thermal radiation would instantaneously halt convective motions above 60 km altitude. Although the convection would be less vigorous, convective entrainment still could substantially weaken the overlying stable layer up to the cloud tops at ~65 km altitude.

We then propose the following scenario for explaining the presence of cellular features in the subsolar re-

gion at the cloud tops. In the early morning prior to sunrise, the neutrally stable layer is relatively thin (~5 km) because the primary heat source driving convection (absorption of solar radiation) has been absent for a substantial length of time. Even without absorption of solar radiation, convection occurs on the Venus nightside [*Ingersoll et al.*, 1987]. Nightside convection may be residual motion from strong dayside convection, or it may be driven by absorption of thermal radiation at the cloud base. Nevertheless, solar energy absorption returns after sunrise and drives stronger convective motions, which in turn, thicken the convection layer through penetration and entrainment. Convection continues to become more vigorous as it nears the subsolar point and the thickness of the convection layer continues to increase. As it passes the location of maximum solar heating (the subsolar point), the convection layer has entrained much of the overlying stable layer and finally expresses itself at the cloud tops. The magnitude of solar heating now starts to decrease, but the convection layer depth does not decrease until longwave radiation has stabilized the atmosphere just below the cloud tops. Thus cellular features exist at the cloud tops well into the afternoon and early evening. This process is similar to the diurnal growth of Earth's planetary boundary layer [*Stull*, 1988]. Recovery of the stable layer on the nightside from 55 to 60 km altitude is not well understood. However, reduction in the vigor of convection is likely a key component. With the major cause of stable layer erosion diminished on the nightside, processes such as infrared heating and cooling that produced the stable layer in the first place become dominant and the stable layer recovers.

Even after deep convection fully develops in the high Ra_q simulations, substantial convective entrainment persists. Strong downdrafts develop from mergers of weaker downwellings. As the weaker downwellings combine, they often trap warmer air between them and transport this buoyant material downward. Warm, entrained air may travel the entire depth of the convection layer.

Convective penetration is significantly deeper for high Rayleigh number convection. The moderate Ra_q simulation experiences average penetration to 42.7 km altitude, while high Ra_q convection overshoots over a scale height to 38.0 km altitude. Such deep convective penetration may have a dramatic influence on dynamics in the lower atmosphere. Penetrative plumes transport heat downward from cloud levels. In fact, downward convective heat flux due to penetration is comparable in magnitude to the solar heat flux at 45 km altitude in our high Ra_q simulations. Heating associated with downward convective heat flux in the penetrative region is largely balanced by cooling associated with upward turbulent (eddy diffusive) heat flux [*Baker et al.*, 1998], and thus convective penetration tends to generate small-scale turbulence in the penetrative region. Convective penetration tends to destabilize the underlying stable layer by producing pockets of warm air embedded within relatively cold air. As our simulations show, this destabilization may be as large as 2 K km^{-1}. The modified static stability will influence the frequencies of internal gravity waves that may exist in the lower atmosphere. Furthermore, internal gravity waves generated by cloud-level penetrative convection will be vertically trapped from 30 to 46 km altitude by the cloud-level convection layer and a lower convection layer from 18 to 30 km altitude [*Sciff et al.*, 1980]. These ducted waves will propagate horizontally and may transfer momentum and energy away from the subsolar region to other locations on the planet. The amount of momentum and energy available for wave transport is closely related to the strength of wave forcing, i.e., the velocity of convective downdrafts and the extent of convective penetration. Further investigations are required to determine the relationship between convective penetration and momentum transport by convectively generated internal gravity waves in Venus' atmosphere.

Strong penetration by convective downdrafts may help explain turbulence observed at 45 km altitude. Radio scintillations in Pioneer Venus radio occultation data indicate two "turbulent" regions, one at 45 km altitude and the other at 60 km altitude [*Woo et al.*, 1980, 1982]. Turbulence generated by wind-shear instability [*Woo et al.*, 1980; *Woo and Ishimaru*, 1981; *Woo et al.*, 1982] and trapped gravity waves [*Woo et al.*, 1980, 1982; *Leroy and Ingersoll*, 1996] have previously been suggested to produce radio scintillations at these altitudes. Recently, vertically propagating internal gravity waves were proposed to account for scintillations observed near 45 km and 60 km altitude in Magellan radio occultation data [*Hinson and Jenkins*, 1995]. However, "turbulence" at 45 km altitude could also be caused by deep penetrative convection. Our simulations indicate that horizontally averaged pressure work near 45 km altitude induced by penetrating plumes is comparable in value to solar heating at that altitude, and local compression regions near penetrating plume heads have values of pressure work 1–2 orders of magnitude larger. Compressional heating may create local gradients in buoyancy and hence decrease the local Richardson number to values less than the critical value of 0.25. Similarly, large vortices associated with penetrating plume heads may generate strong local wind shear and produce turbulent motions.

Convective turbulence with a spectral power law relationship of k^{-3} is present in the high Rayleigh number simulations. Although our calculations are two-dimensional and k^{-3} behavior does occur for 2-D turbulence, the correlation of forcing wavenumbers with the k^{-3} wavenumber range precludes 2-D turbulence as solely responsible for the spectral energy fall-off. Two-dimensional effects still likely occur (note the hint of an anticascade of power to low wavenumber in Figure 8d); however, turbulence generation by buoyancy most likely

controls the spectrum at intermediate wavenumbers. Simple scaling arguments suggest that convective turbulence exhibits k^{-3} behavior in the buoyancy subrange (the range of wavenumbers where buoyancy is the primary cause of vorticity generation and dissipation). It is interesting to note that the k^{-3} behavior occurs over a decade of wavenumbers in the vertical velocity spectrum, but exists over a very limited wavenumber range (if at all) in the potential temperature spectrum. Perhaps our high Ra_q simulations are in a transitional state to convective turbulence, and higher Rayleigh number calculations may possibly show definitive k^{-3} behavior in both vertical velocity and potential temperature. Still, three-dimensional numerical simulations of turbulent convection are needed to more fully reveal the preferred planform, extent of penetration and entrainment, and turbulent structure of cloud-level convection in Venus' atmosphere.

Appendix: Detailed Model Description

A1. Model Equations

The equations for conservation of mass, momentum, and internal energy describe fluid flow and heat transfer in a compressible fluid. The fully compressible equations are required since convection may span multiple scale heights in Venus' atmosphere [*Seiff et al.*, 1980; *Schubert*, 1983] and local compressional work may modify the extent of penetration [*Hurlburt et al.*, 1986]. Rotational effects are neglected since the Coriolis force on Venus is small compared to the inertial force [*Schubert*, 1983]. In addition, latent heating by evaporation and condensation is negligible because mass loading by Venus clouds is insignificant [*Knollenburg and Hunten*, 1980; *Knollenburg et al.*, 1980]. Absorption of solar radiation drives convective motions in our model, and small-scale turbulence is parameterized through isotropic eddy diffusion. In Cartesian geometry, the conservation equations are

$$\frac{\partial \rho}{\partial t} = -\frac{\partial}{\partial x_i}(\rho u_i), \tag{A1}$$

$$\frac{\partial}{\partial t}(\rho u_i) = -\frac{\partial}{\partial x_j}(\rho u_i u_j + p\delta_{ij} - \tau_{ij}) - \rho g \delta_{i3} + S_u, \tag{A2}$$

$$\rho c_p \frac{\partial \theta}{\partial t} = -\rho c_p \frac{\partial}{\partial x_i}(\theta u_i) + \rho c_p \theta \frac{\partial u_i}{\partial x_i} + \frac{\partial}{\partial x_i}\left(\rho c_p \kappa_\theta \frac{\partial \theta}{\partial x_i}\right) + \tau_{ij}\frac{\partial u_j}{\partial x_i} + Q + S_\theta, \tag{A3}$$

where u_i is velocity in the x_i direction, p is pressure, ρ is density, θ is potential temperature, t is time, g is the acceleration of gravity, c_p is the specific heat at constant pressure, κ_θ is thermal eddy diffusivity, and Q is volumetric internal heating. The terms S_u and S_θ represent "steady" processes such as large-scale dynamics and thermal radiation that influence the vertical structure of the atmosphere but operate on timescales much longer than convection and waves. The viscous eddy stress tensor τ_{ij} is given by

$$\tau_{ij} = \rho \kappa_m \left(\frac{\partial u_i}{\partial x_j} + \frac{\partial u_j}{\partial x_i}\right). \tag{A4}$$

Here κ_m is the momentum eddy diffusivity of the fluid. The conservation equations are supplemented by an equation of state, which is given by the perfect gas law

$$p = \rho R T, \tag{A5}$$

where R is the gas constant and T is temperature. For a perfect gas, the potential temperature θ is related to the temperature T by

$$\theta = T\left(\frac{p_0}{p}\right)^{\frac{R}{c_p}}, \tag{A6}$$

where p_0 is a reference pressure. The parameters g, c_p, and R are assumed constant. Although the diffusion coefficients are allowed to vary horizontally and vertically in the model formulation, κ_m and κ_θ are constant for all simulations considered here.

Variables in the model are decomposed into two components:

$$\begin{aligned} \rho &= \bar{\rho} + \rho', \\ p &= \bar{p} + p', \\ u_i &= \bar{u}_i + u_i', \\ \theta &= \bar{\theta} + \theta', \\ Q &= \bar{Q} + Q', \end{aligned} \tag{A7}$$

where quantities with overbars indicate a steady, background state and primed quantities are time-dependent deviations from the background state. The background state is supported by processes that operate on timescales much longer than the rapid variations due to convection and small-scale waves in Venus' atmosphere. For example, thermal radiation below 60 km altitude has a characteristic timescale of 200 days to 52 years [*Pollack and Young*, 1975], while convection and gravity waves operate on timescales of hours to days [*Rossow et al.*, 1980; *Ingersoll et al.*, 1987; *Toigo et al.*, 1994]. As far as convection and small-scale waves are concerned, thermal radiation in the Venus atmosphere below 60 km altitude is a quasi-steady process. However, thermal radiation does influence the thermal structure; the stable layer between the two convection layers is possibly caused by absorption of infrared radiation from the

deep atmosphere at the cloud base [*Seiff*, 1983]. This long-term influence of thermal radiation is incorporated into the background state. Similarly, large-scale dynamics such as Hadley circulations may contribute to the vertical structure of the Venus atmosphere. Stable lapse rates are inherently required for Hadley cells to transport heat poleward [*Stone*, 1974]. Processes such as thermal radiation and large-scale dynamics that support the background state are formally represented in equations (A1)–(A3) by S_u and S_θ.

The background state is steady and hydrostatic; it varies only with altitude z. The equations for the background state are given by

$$\frac{d}{dz}\left(\bar{\rho}\kappa_m \frac{d\bar{u}}{dz}\right) + S_u = 0, \tag{A8}$$

$$\frac{d\bar{p}}{dz} = -\bar{\rho}g, \tag{A9}$$

$$\frac{d}{dz}\left(\bar{\rho}c_p\kappa_\theta \frac{d\bar{\theta}}{dz}\right) + \bar{\rho}\kappa_m\left(\frac{d\bar{u}}{dz}\right)^2 + S_\theta = 0, \tag{A10}$$

where $\bar{u}$ is the mean horizontal wind of the background state. For the simulations reported here, the mean horizontal wind $\bar{u}$ is taken to be zero. The background state equations are not formally solved in our model. Rather, a mean thermal structure based on Pioneer Venus probe data is implemented to describe the Venus background state (Figure 1). The profile of static stability is similar to that used by *Young et al.* [1987].

Substitution of equations (A7) into conservation equations (A1)–(A3) and subtraction of the steady background state equations (A8)–(A10) gives

$$\frac{\partial \rho'}{\partial t} = -\frac{\partial}{\partial x_i}(\rho u_i'), \tag{A11}$$

$$\frac{\partial}{\partial t}(\rho u_i') = -\frac{\partial}{\partial x_j}(\rho\bar{u}_i u_j' + \rho u_i'\bar{u}_j + \rho u_i' u_j' + p'\delta_{ij} - \tau_{ij}') - \rho' g\delta_{i3}, \tag{A12}$$

$$\rho c_p \frac{\partial \theta'}{\partial t} = -\rho c_p \frac{\partial}{\partial x_i}\left(\bar{\theta}u_i' + \theta'\bar{u}_i + \theta' u_i'\right) + \rho c_p(\bar{\theta} + \theta')\frac{\partial u_i'}{\partial x_i} + \frac{\partial}{\partial x_i}\left(\rho c_p \kappa_\theta \frac{\partial \theta'}{\partial x_i}\right) + \bar{\tau}_{ij}\frac{\partial u_j'}{\partial x_i} + \tau_{ij}'\frac{\partial \bar{u}_j}{\partial x_i} + \tau_{ij}'\frac{\partial u_j'}{\partial x_i} + Q'. \tag{A13}$$

We prefer to call this set of equations the "deviation" conservation equations rather than the conventional "perturbation" equations because "perturbation" implies a small deviation from the background state. Deviations may, in fact, be quite large in amplitude.

A2. Numerical Method and Code Testing

For the numerical simulations presented here, we utilize parallel supercomputers which contain many (currently from 24 to 1024) processors that operate on distributed data simultaneously rather than in sequential order as traditional vector supercomputers do. The code, written in High Performance Fortran (HPF) and CM-Fortran (a version of HPF for the Connection Machine CM-5), runs on a variety of parallel platforms including the Connection Machine CM-5, the IBM SP-2, the SGI PowerChallenge Array, and the Cray T3E. It utilizes the SPMD (Single Program–Multiple Data) paradigm in which the data are distributed throughout the processors and single instructions operate simultaneously on all data in the machine. In general, computational costs are more expensive for communication between processors than for data processing at the same processor. Thus numerical methods must be chosen carefully to minimize communication between processors [e.g., *Leiss*, 1995].

The numerical model is a finite difference code with second-order accuracy in space and time. Spatial derivatives are computed using centered second-order differences which use information only from neighboring gridpoints and thus helps to minimize communication between processors. A vertically staggered grid is implemented to more accurately account for vertical fluxes [*Haltiner and Williams*, 1980]. For all terms but the diffusion terms, the solutions are advanced in time using an explicit second-order time-adaptive (variable time step) leapfrog scheme. The leapfrog scheme is commonly used in convection and gravity wave studies [e.g., *Deardorff*, 1972; *Klemp and Wilhelmson*, 1978; *Eidson*, 1985; *Tao and Simpson*, 1993; *Young et al.*, 1994] because of numerical stability for advection terms, lack of amplitude dissipation, and ease of implementation [*Arakawa*, 1966; *Haltiner and Williams*, 1980; *Press et al.*, 1989]. However, the leapfrog scheme is unconditionally unstable for diffusion terms, so other schemes must be implemented for these terms. Two different schemes are used for diffusion terms to strike a balance between computational efficiency and second-order accuracy. The thermal diffusion term is integrated forward in time using an implicit Crank-Nicolson scheme. Direct matrix solvers for parallel machines, although dramatically improved in recent years, typically do not work well since global communication between processors is required. Instead, an iterative Jacobi method is used to solve the matrix equation. Jacobi iteration experiences slow convergence on serial platforms, but this method is rather efficient on parallel machines because Jacobi matrix multiplications involve only nearest neighbor communications [*Jones*, 1991]. Momentum diffusion terms are solved explicitly using a first-order Euler time-lag scheme. The time-lag scheme has been used successfully to solve diffusion terms in many convection studies [e.g., *Deardorff*, 1972; *Eidson*, 1985;

Table A1. Convection Benchmark Tests of HPF Code

Benchmark	Ra/Ra_c	Nu	Nu_{code}	M	M_{code}	P	P_{code}
Thirby [1970]	10.8	2.4	2.4	—	0.01	0.0	0.0
Moore and Weiss [1973]	200	11.4	11.1	—	0.04	3.6	3.7
Graham [1975] Z=1	10	4.2	4.3	0.11	0.10	0.0	0.0
Graham [1975] Z=4	10	3.4	3.5	0.19	0.18	0.0	0.0

Muthsam et al., 1995]. As we show below, the first-order scheme does not, in practice, limit the second-order accuracy of our convection simulations. In addition, we employ the time-smoothing filter of *Asselin* [1972] to dampen the leapfrog computational mode.

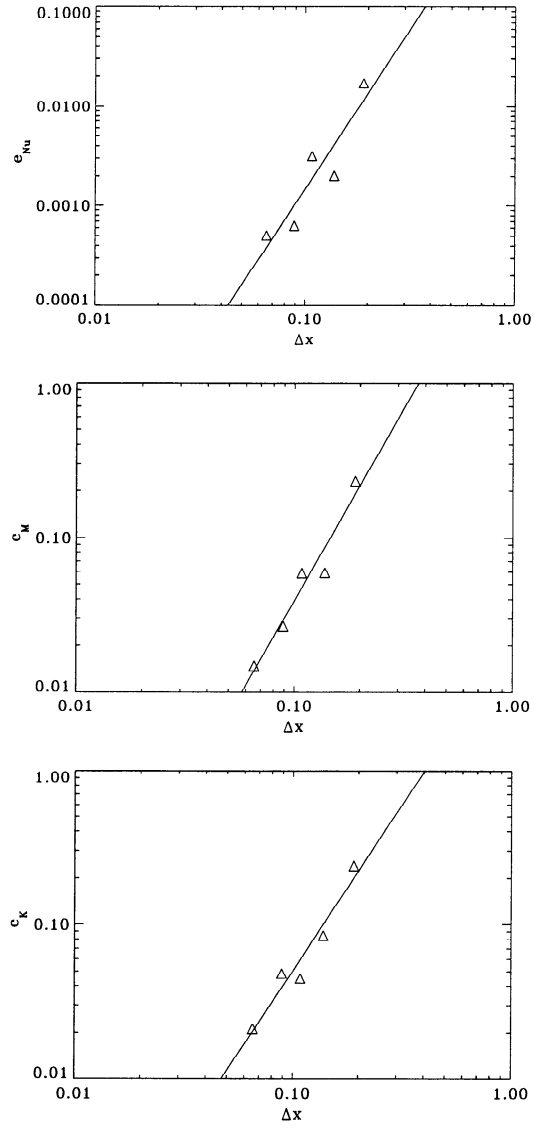

Figure A1. Resolution tests of the IIPF code for the *Thirby* [1970] internally heated case. The upper, middle, and lower panels show the relative error e_{Nu}, e_M, and e_K associated with Nu, M, and K, respectively. Triangles represent the measured relative error, and solid lines indicate least squares power law fits with power law exponents of 3.2, 2.5, and 2.1, respectively. The grid spacing Δx is nondimensional.

The HPF code has been tested extensively against previous numerical results and for numerical consistency and accuracy. Table A1 lists benchmark results against four previous convection simulations. The *Thirby* [1970] case is a Boussinesq, purely internally heated case with a steady solution, and the *Moore and Weiss* [1973] case is a Boussinesq, bottom heated calculation with time-dependent behavior. The two steady, bottom heated, fully compressible cases of *Graham* [1975] exhibit different degrees of density stratification. The nondimensional parameter $Z = (T_l - T_u)/T_u$ used by Graham, where T_l is the temperature at the lower boundary and T_u is the temperature at the upper boundary, is a measure of the layer thickness. The Rayleigh number Ra in Table A1 is either the bottom heated Rayleigh number or the internally heated Rayleigh number, depending on the specific case, and Ra_c is the critical Rayleigh number for the onset of convection. Specific quantities compared include the Nusselt number Nu (the nondimensional heat flux), the Mach number M, and the period P of time-dependent oscillations in Nu. As Table A1 indicates, our fully compressible HPF code results agree quite well with previous steady and time-dependent numerical results. In all cases, the flow patterns produced by the HPF code match the benchmark flow patterns.

Numerical consistency is confirmed through resolution tests of the *Thirby* [1970] internally heated case. Figure A1 shows the relative error e_{Nu}, e_M, and e_K (associated with Nu, M, and the domain-averaged kinetic energy density K, respectively) as a function of grid spacing Δx (and hence time step Δt, since the size of the time step is determined from the Courant condition). The "correct" values of Nu, M, and K are estimated using Richardson extrapolation. For all three quantities, the relative error decreases as the grid spacing decreases, thereby indicating numerical consistency. In addition, the solutions with different resolutions have similar flow patterns and match the flow pattern (steady convective rolls) of *Thirby* [1970].

Furthermore, least squares power law fits of the relative error indicate that the effective accuracy of the code is second-order. As discussed earlier, the momentum diffusion terms are solved with a first-order time-lag scheme. For problems in which momentum diffusion is a dominant process, the accuracy of the code is likely limited by the accuracy of the momentum diffusion

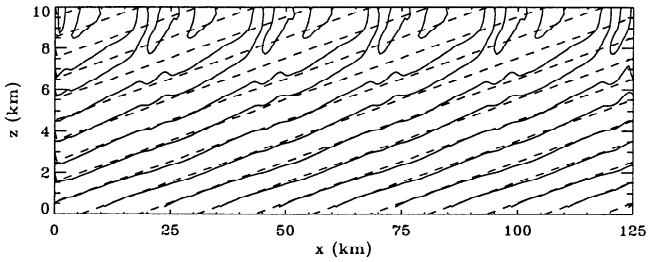

Figure A2. Comparison of numerical results (solid) and analytical results (dashed) for the gravity wave test case. The zero contour of vertical velocity is shown for time $t = 20.2$ hours. The sponge layer influences gravity wave wavelengths and propagation above 5 km altitude.

Table A2. Gravity Wave Test Case

Quantity	Value
N	1.785×10^{-2} s^{-1}
ω_a	1.976×10^{-2} s^{-1}
c	347 m s^{-1}
w_0	0.40 m s^{-1}
k	2.513×10^{-4} m^{-1}
l_x	25 km
ω	1.423×10^{-3} s^{-1}
P	73 min
c_x	5.7 m s^{-1}

terms. The low Rayleigh number calculation of *Thirby* [1970] offers an excellent test of the influence of the first-order time-lag scheme on the overall accuracy of the code since diffusion terms are relatively important. In resolution tests of the *Thirby* [1970] case, the Nusselt number Nu experiences $(\Delta x)^{3.2}$ convergence, the Mach number M shows $(\Delta x)^{2.5}$ convergence, and the kinetic energy K has $(\Delta x)^{2.1}$ convergence (Figure A1). Thus, second-order accuracy of the code is observed even in situations where diffusion is strong. The momentum diffusion terms do not limit the overall accuracy of the code probably because the time step is determined by advection terms and therefore diffusive processes are temporally well-resolved.

The ability of the code to accurately simulate gravity wave propagation has also been confirmed (Figure A2). For this test, gravity waves in an isothermal atmosphere are continually forced at the bottom boundary by a forcing function of the form $w = w_0 \cos(kx - \omega t)$, where w is vertical velocity, w_0 is vertical velocity wave amplitude, k is the horizontal wavenumber in the x direction, ω is the angular frequency, and t is time. The horizontal extent is 125 km, and the vertical extent is 10 km. The side boundaries are periodic. A sponge layer with an exponential scale height of 2.3 km exists near the top of the domain to prevent gravity wave reflection. Table A2 provides further specifics of the gravity wave test case, where N is the Brunt-Väisälä frequency, ω_a is the acoustic cutoff frequency, c is the sound speed, l_x is the horizontal wavelength, P is wave period, and c_x is the horizontal phase speed. Numerical results are compared to an analytical solution [*Houghton*, 1986] given by

$$w = w_0 e^{z/2H} \cos(kx - mz - \omega t) \qquad \text{(A14)}$$

where m is the vertical wavenumber, z is altitude, and H is the pressure scale height. The vertical wavenumber m is related to the horizontal wavenumber k and angular frequency ω by

$$m^2 = \left(\frac{N^2}{\omega^2} - 1\right)k^2 + \frac{(\omega^2 - \omega_a^2)}{c^2} \qquad \text{(A15)}$$

As Figure A2 shows, numerical results agree quite well with the analytical solution. Horizontal wavelengths, vertical wavelengths, and phase propagation coincide with the analytical solution below 5 km altitude. Numerical wave amplitudes of $w \sim 0.39$ m s^{-1} (corrected for variation of amplitude with altitude) also compare well with the analytical value of $w_0 = 0.40$ m s^{-1}. Above 5 km altitude, the sponge layer modifies horizontal and vertical wavelengths and strongly dampens gravity wave amplitudes.

Acknowledgments. This work was supported under grants NAGW-1874 and NAG5-4117 from the NASA Planetary Atmospheres Program. The calculations were performed on the CM-5 at the National Center for Supercomputing Applications, University of Illinois at Urbana-Champaign and the NPACI Cray T3E at the San Diego Supercomputing Center.

References

Arakawa, A., Computational design for long term integration of the equations of fluid motion: Two-dimensional incompressible flow, Part I, *J. Comput. Phys.*, *1*, 119–143, 1966.

Asselin, R., Frequency filter for time integrations, *Mon. Weather Rev.*, *100*, 487–490, 1972.

Baker, R. D., and G. Schubert, Cellular convection in the atmosphere of Venus, *Nature*, *355*, 710–712, 1992.

Baker, R. D., G. Schubert, and P. W. Jones, Cloud-level penetrative compressible convection in the Venus atmosphere, *J. Atmos. Sci.*, *55*, 3–18, 1998.

Belton, M. J. S., G. R. Smith, G. Schubert, and A. D. Del Genio, Cloud patterns, waves and convection in the Venus atmosphere, *J. Atmos. Sci.*, *33*, 1394–1417, 1976.

Belton, M. J. S., et al., Images from Galileo of the Venus cloud deck, *Science*, *253*, 1531–1536, 1991.

Berkowicz, R., Spectral methods for atmospheric diffusion modeling, *Boundary Layer Meteorol.*, *30*, 201–220, 1984.

Blix, T. A., et al., Small-scale structure observed in-situ during MAC/EPSILON, *J. Atmos. Terr. Phys.*, *52*, 835–854, 1990.

Chandrasekhar, S., *Hydrodynamic and Hydromagnetic Stability*, Dover, New York, 1961.

Covey, C., and G. Schubert, Mesoscale cellular convection in the clouds of Venus, *Nature*, *290*, 17–20, 1981.

Deardorff, J. W., Numerical investigation of neutral and unstable planetary boundary layers, *J. Atmos. Sci.*, *29*, 91–115, 1972.

Eidson, T. M., Numerical simulation of the turbulent Rayleigh-Bénard problem using subgrid modelling, *J. Fluid Mech.*, *158*, 245–268, 1985.

Emanuel, K. A., *Atmospheric Convection*, Oxford Univ. Press, New York, 1994.

Gierasch, P. J., Waves in the atmosphere of Venus, *Nature*, *328*, 510–512, 1987.

Graham, E., Numerical simulation of two-dimensional compressible convection, *J. Fluid Mech.*, *70*, 689–703, 1975.

Haltiner, G. J., and R. T. Williams, *Numerical Prediction and Dynamic Meteorology*, 2nd ed., John Wiley, New York, 1980.

Hinson, D. P., and J. M. Jenkins, Magellan radio occultation measurements of atmospheric waves on Venus, *Icarus*, *114*, 310–327, 1995.

Hou, A. Y., and R. M. Goody, Further studies of the circulation of the Venus atmosphere, *J. Atmos. Sci.*, *46*, 991–1001, 1989.

Houghton, J. T., *The Physics of Atmospheres*, 2nd ed., Cambridge Univ. Press, New York, 1986.

Hurlburt, N. E., J. Toomre, and J. M. Massaguer, Two-dimensional compressible convection extending over multiple scale heights, *Astrophys. J.*, *282*, 557–573, 1984.

Hurlburt, N. E., J. Toomre, and J. M. Massaguer, Nonlinear compressible convection penetrating into stable layers and producing internal gravity waves, *Astrophys. J.*, *311*, 563–577, 1986.

Ingersoll, A. P., D. Crisp, A. W. Grossman, and the VEGA Balloon Science Team, Estimates of convective heat fluxes and gravity wave amplitudes in the Venus middle cloud layer from Vega balloon measurements, *Adv. Space. Res.*, 7, (12)343–(12)349, 1987.

James, E. P., O. B. Toon and G. Schubert, A numerical microphysical model of the condensational Venus cloud, *Icarus*,*129*, 147–171, 1997.

Jenkins, J. M., P. G. Steffes, D. P. Hinson, J. D. Twicken, and G. L. Tyler, Radio occultation studies of the Venus atmosphere with the Magellan spacecraft, Results from the October 1991 experiments, *Icarus*, *110*, 79–94, 1994.

Jones, P. W., Compressible convection and pulsations on parallel computers, Ph.D. thesis, Univ. of Colo., Boulder, 1991.

Kerr, R. M., Rayleigh number scaling in numerical convection, *J. Fluid Mech.*, *310*, 139–179, 1996.

Klemp, J. B., and R. B. Wilhelmson, The simulation of three-dimensional convective storm dynamics, *J. Atmos. Sci.*, *35*, 1070–1096, 1978.

Knollenburg, R. G., and D. M. Hunten, The microphysics of the clouds of Venus: Results of the Pioneer Venus particle size spectrometer experiment, *J. Geophys. Res.*, *85*, 8039–8058, 1980.

Knollenburg, R. G., L. Travis, M. Tomasko, P. Smith, B. Ragent, L. Esposito, D. McCleese, J. Martonchik, and R. Beer, The clouds of Venus: A synthesis report, *J. Geophys. Res.*, *85*, 8059–8081, 1980.

Kolmogorov, A. N., Energy dissipation in locally isotropic turbulence, *Dokl. Akad. Nauk SSSR*, *32*, 19–21, 1941.

Kotsovinos, N. E., Turbulence spectra in free convection flow, *Phys. Fluids A*, *3*, 163–167, 1991.

Kraichnan, R. H., Inertial ranges in two-dimensional turbulence, *Phys. Fluids*, *10*, 1417–1423, 1967.

Krasnopolsky, V. A., Chemical composition of Venus clouds, *Planet. Space Sci.*, *33*, 109–117, 1985.

Krasnopolsky, V. A., and V. A. Parshev, Chemical composition of the atmosphere of Venus, *Nature*, *292*, 610–613, 1981.

Krasnopolsky, V. A., and V. A. Parshev, Photochemistry of the Venus atmosphere, in *Venus*, edited by D. M. Hunten, L. Colin, T. M. Donahue, and V. I. Moroz, pp. 431–458, Univ. of Ariz. Press, Tucson, 1983.

Leiss, E. L., *Parallel and Vector Computing: A Practical Introduction*, McGraw-Hill, New York, 1995.

Leroy, S. S., Convectively generated internal gravity waves in Venus's middle atmosphere: Momentum transport and radio scintillations, Ph.D. thesis, Cal. Inst. of Technol., Pasadena, 1994.

Leroy, S. S., and A. P. Ingersoll, Convective generation of gravity waves in Venus's atmosphere: Gravity wave spectrum and momentum transport, *J. Atmos. Sci.*, *52*, 3717–3737, 1995.

Leroy, S. S., and A. P. Ingersoll, Radio scintillations in Venus's atmosphere: Application of a theory of gravity wave generation, *J. Atmos. Sci.*, *53*, 1018–1028, 1996.

Lilly, D. K., Numerical simulation of two-dimensional turbulence, *Phys. Fluids, Suppl. II*, 240–249, 1969.

Lumley, J. L., The spectrum of nearly inertial turbulence in a stably stratified fluid, *J. Atmos. Sci.*, *21*, 99–102, 1964.

Maddox, R. A., Mesoscale convective complexes, *Bull. Am. Meteorol. Soc.*, *61*, 1374–1387, 1980.

Mason, P. J., Large-eddy simulation of the convective atmospheric boundary layer, *J. Atmos. Sci.*, *46*, 1492–1516, 1989.

Moore, D. R., and N. O. Weiss, Two-dimensional Rayleigh–Bénard convection, *J. Fluid Mech.*, *58*, 289–312, 1973.

Murray, B. C., et al., Venus: Atmospheric motion and structure from Mariner 10 pictures, *Science*, *183*, 1307–1315, 1974.

Muthsam, H. J., W. Gob, F. Kupka, W. Liebich, and J. Zochling, A numerical study of compressible convection, *Astron. Astrophys.*, *293*, 127–141, 1995.

Pollack, J. B., and R. Young, Calculations of the radiative and dynamical state of the Venus atmosphere, *J. Atmos. Sci.*, *32*, 1025–1037, 1975.

Press, W. H., B. P. Flannery, S. A. Teukolsky, and W. T. Vetterling, *Numerical Recipes: The Art of Scientific Computing (Fortran Version)*, Cambridge Univ. Press, New York, 1989.

Roberts, P. H., Convection in horizontal layers with internal heat generation, Theory, *J. Fluid Mech.*, *30*, 33–49, 1967.

Rossow, W. B., A. D. Del Genio, S. S. Limaye, L. D. Travis, and P. H. Stone, Cloud morphology and motions from Pioneer Venus images, *J. Geophys. Res.*, *85*, 8107–8128, 1980.

Schinder, P. J., P. J. Gierasch, S. S. Leroy, and M. D. Smith, Waves, advection, and cloud patterns on Venus, *J. Atmos. Sci.*, *47*, 2037–2052, 1990.

Schubert, G., General circulation and the dynamical state of the Venus atmosphere, in *Venus*, edited by D. M. Hunten, L. Colin, T. M. Donahue, and V. I. Moroz, pp. 681–765, Univ. of Ariz. Press, Tucson, 1983.

Seiff, A., Thermal structure of the atmosphere of Venus, in *Venus*, edited by D. M. Hunten, L. Colin, T. M. Donahue, and V. I. Moroz, pp. 215 279, Univ. of Ariz. Press, Tucson, 1983.

Seiff, A., D. B. Kirk, R. E. Young, R. C. Blanchard, J. T. Findlay, G. M. Kelly, and S. C. Sommer, Measurements of thermal structure and thermal contrasts in the atmosphere of Venus and related dynamical observations: Results from the four Pioneer Venus probes, *J. Geophys. Res.*, *85*, 7903–7933, 1980.

Shao, Q., and D. A. Randall, Closed mesoscale cellular convection driven by cloud-top radiative cooling, *J. Atmos. Sci.*, *53*, 2144–2165, 1996.

Stone, P. H., The structure and circulation of the deep Venus atmosphere, *J. Atmos. Sci.*, *31*, 1681–1690, 1974.

Stull, R. B., The energetics of entrainment across a density interface, *J. Atmos. Sci.*, *33*, 1260–1267, 1976.

Stull, R. B., *An Introduction to Boundary Layer Meteorology*, Kluwer Acad., Boston, 1988.

Tao, W.-K., and J. Simpson, Goddard Cumulus Ensemble Model, Part I, Model description, *Terr. Atmos. Oceanic Sci.*, *4*, 35–72, 1993.

Thirby, R., Convection in an internally-heated fluid, *J. Fluid Mech.*, *44*, 673–693, 1970.

Toigo, A., P. J. Gierasch, and M. D. Smith, High resolution cloud feature tracking on Venus by Galileo, *Icarus*, *109*, 318–336, 1994.

Tomasko, M. G., L. R. Doose, P. H. Smith, and A. P. Odell, Measurements of the flux of sunlight in the atmosphere of Venus, *J. Geophys. Res.*, *85*, 8167–8186, 1980.

Turner, J. S., *Buoyancy Effects in Fluids*, Cambridge Univ. Press, New York, 1973.

Woo, R., and A. Ishimaru, Eddy diffusion coefficient for the atmosphere of Venus from radio scintillation measurements, *Nature*, *289*, 383–384, 1981.

Woo, R., J. W. Armstrong, and A. Ishimaru, Radio occultation measurements of turbulence in the Venus atmosphere by Pioneer Venus, *J. Geophys. Res.*, *85*, 8031–8038, 1980.

Woo, R., J. W. Armstrong, and A. J. Kliore, Small-scale turbulence in the atmosphere of Venus, *Icarus*, *52*, 335–345, 1982.

Young, R. E., R. L. Walterscheid, G. Schubert, A. Seiff, V. M. Linkin, and A. N. Lipatov, Characteristics of gravity waves generated by surface topography on Venus: Comparison with the Vega balloon results, *J. Atmos. Sci.*, *44*, 2628–2639, 1987.

Young, R. E., R. L. Walterscheid, G. Schubert, L. Pfister, H. Houben, and D. L. Bindschadler, Characteristics of finite amplitude stationary gravity waves in the atmosphere of Venus, *J. Atmos. Sci.*, *51*, 1857–1875, 1994.

Yung, Y. L., and W. B. Demore, Photochemistry of the stratosphere of Venus: Implications for atmospheric evolution, *Icarus*, *51*, 199–247, 1982.

R. D. Baker, Mesoscale Atmospheric Processes Branch, Code 912, NASA Goddard Space Flight Center, Greenbelt, MD 20771. (rbaker@agnes.gsfc.nasa.gov)

P. W. Jones, Theoretical Division, Los Alamos National Laboratory, Los Alamos, New Mexico 87545. (pwjones@lanl.gov)

G. Schubert, Department of Earth and Space Sciences, 3806 Geology Building, Box 951567, University of California, Los Angeles, CA 90095-1567. (schubert@ucla.edu)

(Received July 17, 1998; revised October 21, 1998; accepted November 2, 1998.)